ELSEVIER

Ceramics International 31 (2005) 1–9

CERAMICS INTERNATIONAL

www.elsevier.com/locate/ceramint

Deformed microstructure in pressureless-sintered barium titanate

Jing-Kae Liou[1], Hong-Yang Lu*

Centre for Nanoscience, Institute of Materials Science and Engineering, National Sun Yat-Sen University, Kaohsiung 80424, Taiwan

Received 23 November 2003; received in revised form 21 January 2004; accepted 19 February 2004
Available online 26 June 2004

Abstract

The sintered microstructure of pressureless-sintered $BaTiO_3$ analysed by transmission electron microscopy (TEM) reveals that plastic deformation occurred at 1400 °C when the slip systems of $\langle 1\,\bar{1}\,0\rangle\{1\,1\,0\}$, $\langle 1\,0\,0\rangle\{1\,1\,0\}$ and $\langle 100\rangle\{0\,0\,1\}$ were activated by the intrinsic sintering stress (Σ). Dislocations with the Burgers vectors $\boldsymbol{b}_1 = \langle 1\,1\,0\rangle$ and $\boldsymbol{b}_1' = \langle 1\,0\,0\rangle$ have dissociated. The dissociation reactions of $\boldsymbol{b}_1 = \boldsymbol{b}_2 + \boldsymbol{b}_3$ are: $[1\,0\,1] \rightarrow [0\,0\,1] + [1\,0\,0]$ and $[0\,0\,1] \rightarrow 1/2[1\,0\,1] + 1/2[\bar{1}\,0\,1]$, respectively. Both dissociated dislocations contained a series of scallop-shaped half-loop partials with the Burgers vectors respectively of $\boldsymbol{b}_3 = [1\,0\,0]$ and $\boldsymbol{b}_3' = 1/2[\bar{1}\,0\,1]$. The dissociations took place by a climb mechanism. Polygonisation in dynamic recovery, necessitating both glide and climb of dislocations, occurred during sintering at 1400 °C, and which is clearly evidenced by sub-grain formation. Densification was contributed by dislocation mechanisms where the ceramic has been plastically deformed by the sintering stress. Densification of the undoped and Sr-doped $BaTiO_3$ compositions by pressureless-sintering in relation to the dislocation substructure is discussed.

Keywords: A. Sintering; B. Electron microscopy; B. Microstructure-final; D. $BaTiO_3$ and titanates; D. Perovskites; Dislocations

1. Introduction

$BaTiO_3$ perovskite is a ferroelectric ceramic used extensively in the electronic industries. Sintering of $BaTiO_3$ powder, made to a green body, is usually adopted to manufacture the passive components, e.g. dielectric capacitors. Dislocation mechanisms have long been suggested [1] to be an important contribution to the densification of ceramics. However, deformed microstructure in sintered ceramics has seldom been analysed in correlation to sintering at high temperatures.

It is also known [2–5] that the lower mantle of the earth being more silicic than the higher mantle is constituted predominantly of pyroxene $(Mg,Fe)SiO_3$ with the perovskite structure. The viscosity of the lower mantle may be investigated by looking into the plastic deformation of the perovskites [3] at high temperatures. Indeed, $BaTiO_3$ [7] and other perovskites [6–10] have been taken as model materials in understanding dislocation creep in the earth mantle.

All crystallographic indices here refer to the cubic structure, taking the tetragonal $BaTiO_3$ of ∼1.01 as pseudo-cubic [7]. Two types of dislocations with the Burgers vectors $\boldsymbol{b}_1 = \langle 1\,0\,0\rangle$ and $\langle 1\,1\,0\rangle$ were determined in the perovskites of $KTaO_3$ [4], $KZnF_3$ [6], $CaTiO_3$ [7], $BaTiO_3$ [7], $SrTiO_3$ [8,9] and $CaGeO_3$ [10], often taken as model materials to simulate deformation in the lower mantle. The $\langle 1\,\bar{1}\,0\rangle\{1\,1\,0\}$ slip systems were common to samples deformed at high temperature and those micro-indented at room temperature. However, the slip systems of $\langle 1\,0\,0\rangle\{0\,0\,1\}$ were only observed in $BaTiO_3$ quenched from high temperatures [4]. Both types of the dislocations with $\boldsymbol{b}_1 = \langle 1\,0\,0\rangle$ and $\langle 1\,\bar{1}\,0\rangle$ have been determined in creep-deformed samples of the perovskite structure [4–10].

Grown-in dislocations with $\boldsymbol{b} = \langle 1\,0\,0\rangle$ have dissociated [7,11,12] into a series of half-loop partials in $BaTiO_3$ samples creep-deformed at 1400 °C in air. The half-loop partials resembling the scallop shape [7,11,12] were a characteristic feature to deformed microstructure. Nevertheless, observations by Doukhan and Doukhan [7] were confined to single crystals subjected to creep deformation at 1150–1570 °C before slowly cooled to room temperature. Studies on quenched $BaTiO_3$ samples from CO_2-laser-sintering [13] have confirmed [11,12] that the $\boldsymbol{b} = [0\,0\,1]$ dislocations

* Corresponding author. Tel.: +886-7-5254052; fax: +886-7-5256030.
E-mail address: hyl@mail.nsysu.edu.tw (H.-Y. Lu).
[1] Present address: Lam Research Co., Science-based Industrial Park, Hsinchu 300, Taiwan, ROC.

0272-8842/$30.00 © 2004 Elsevier Ltd and Techna S.r.l. All rights reserved.
doi:10.1016/j.ceramint.2004.02.005

dissociated into half-loop partials [12] as well as two collinear partials [11]. The dissociation into collinear partials has occurred by a mixed mechanism of glide and climb either on (1 1 1) [11] or (1 0 $\bar{1}$) [12] by Lin and Lu in samples sintered in air using CO_2-laser [13], where rapid quenching to room temperature was possible.

Dissociation of dislocations with Burgers vector $\boldsymbol{b}_1$ by the reaction of the type: $\boldsymbol{b}_1 \rightarrow \boldsymbol{b}_2 + \boldsymbol{b}_3$,

$$[0\,1\,0] \rightarrow \tfrac{1}{2}[0\,1\,\bar{1}] + \tfrac{1}{2}[0\,1\,1] \quad (1)$$

has resulted in two partial dislocations with orthogonal $\boldsymbol{b}_2$ and $\boldsymbol{b}_3$. The half-loop partial $\boldsymbol{b}_3 = 1/2[0\,1\,1]$ nucleated at high temperature was dissociated subsequently by climb in (0 1 0) while the other partial segment $\boldsymbol{b}_2 = 1/2[0\,1\,\bar{1}]$ remained stationary [7]. Another segment of the initial dislocation, with Burgers vector $\boldsymbol{b}_1 = [0\,1\,0]$ normal to the half-loop lying in (0 1 0), was not dissociated. However, the microstructure feature is not common in the perovskites taken as model materials, no such half-loop dislocations were detected in $KTaO_3$ [4] or $CaGeO_3$ [10] deformed by high-temperature creep.

Fig. 1 illustrates schematically the dissociation reaction of $\boldsymbol{b} = [0\,1\,0]$ by climb in the (0 1 0) plane [7].

Both types of dislocations, i.e. $\boldsymbol{b}$=⟨1 0 0⟩ and ⟨1 $\bar{1}$ 0⟩, have dissociated into partials by the following reaction, respectively, in $CaGeO_3$.

$$[1\,\bar{1}\,0] \rightarrow \tfrac{1}{2}[1\,\bar{1}\,0] + \tfrac{1}{2}[1\,\bar{1}\,0] \quad (2)$$

$$[0\,0\,1] \rightarrow \tfrac{1}{2}[0\,0\,1] + \tfrac{1}{2}[0\,0\,1] \quad (3)$$

The latter (Eq. (3)) found [11] in CO_2-laser-sintered $BaTiO_3$ has not been reported [4–10] for any other creep-deformed perovskite samples. The dissociated dislocations with $\boldsymbol{b}$=⟨1 0 0⟩ found in $CaGeO_3$ perovskite were in a pure climb configuration [10].

Investigating the microstructure of pressureless-sintered $SrTiO_3$ ceramics, only $\boldsymbol{b}$=⟨1 $\bar{1}$ 0⟩ was reported [9]. It was revealed by weak-beam imaging that $\boldsymbol{b}_1 = [0\,\bar{1}\,1]$ dissociated by pure climb and pure glide via the reaction:

$$[0\,\bar{1}\,1] \rightarrow \tfrac{1}{2}[0\,\bar{1}\,1] + \tfrac{1}{2}[0\,\bar{1}\,1] \quad (4)$$

However, dissociation by the following reaction:

$$[0\,\bar{1}\,1] \rightarrow [0\,\bar{1}\,0] + [0\,0\,1] \quad (5)$$

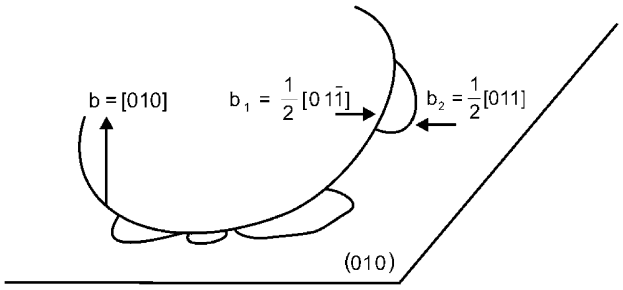

Fig. 1. A schematic illustration of dislocation dissociation by $\boldsymbol{b}_1 = \boldsymbol{b}_2 + \boldsymbol{b}_3$ (redrawn from Ref. [7]).

as suggested by Poirier et al. [4], was not found in sintered $SrTiO_3$ ceramics.

In this study, the microstructure of pressureless-sintered (i.e. sintered in air), undoped and Sr-doped $BaTiO_3$ compositions has been analysed via transmission electron microscopy (TEM). Observations suggest that the glide systems of ⟨1 $\bar{1}$ 0⟩{1 1 0}, ⟨1 0 0⟩{1 1 0} and ⟨1 0 0⟩{0 0 1} [4–12] have been activated when $BaTiO_3$ was sintered at 1400 °C in air. Dislocations dissociated into the scallop-shaped, half-loop partials, and collinear partials by Eqs. (4) and (5), respectively, has occurred. The dissociation reaction by Eq. (5), which has not been unequivocal in the past [7,9], is confirmed.

2. Experimental procedure

Commercially available $BaTiO_3$ powder (with (Ba/Ti) ≈ 0.997, Ticon® HPB, Ferro, Niagara Falls, NY, USA) and $SrTiO_3$ powder (with (Sr/Ti) ≈ 0.999, HPST-1, Fuji Titanium, Kanagawa, Japan) were used for the present study. Both powders containing TiO_2 excess are non-stoichiometric. Powders of appropriate quantities, doped and undoped with $SrTiO_3$, were mixed in isopropyl alcohol (IPA) using Y_2O_3–ZrO_2 balls in a plastic bottle for 2 h. The mixed slurry was then dried at 120 °C for 12 h before deagglomerated using an agate mortar and pestle. The dried powder passed through ~75 μm sieve to exclude large agglomerates was dry-pressed at 100 MPa in a WC-inserted steel die to pellets of ~5 mm in diameter. They were debindered at 700 °C for 6 h before sintered in a conventional tube furnace at 1400 °C in air, followed by furnace-cooling to room temperature.

Sintered samples were sliced with a diamond-embedded saw blade, mechanically ground using SiC grits and polished successively to 1 μm roughness with diamond pastes. Polished sections were either thermally etched at 1200 °C for 30 min or chemically etched with 1% HF solution in order to delineate grain boundaries and the ferroelectric domains. Observations via scanning electron microscopy (SEM) using JEM6400 (JEOL, Tokyo, Japan) were made on Au–Pd-coated specimens. Thin foils were prepared by ultrasonic cutting of the sliced discs to 3 mm in diameter, mechanical polishing to <200 μm thick and dimple-grinding (SBT-515, Southbay Technologies, San Clemente, CA, USA) to <20 μm thick in the centre region before ion-beam thinning (Gatan 600 Duomill™) to electron transparency. They were analysed via TEM using JEOL AEM 3010 microscopes operating at 300 kV.

3. Results

3.1. Crystalline phases

Sintered undoped samples contained predominantly tetragonal (t-)$BaTiO_3$ with a minor amount of the monoclinic

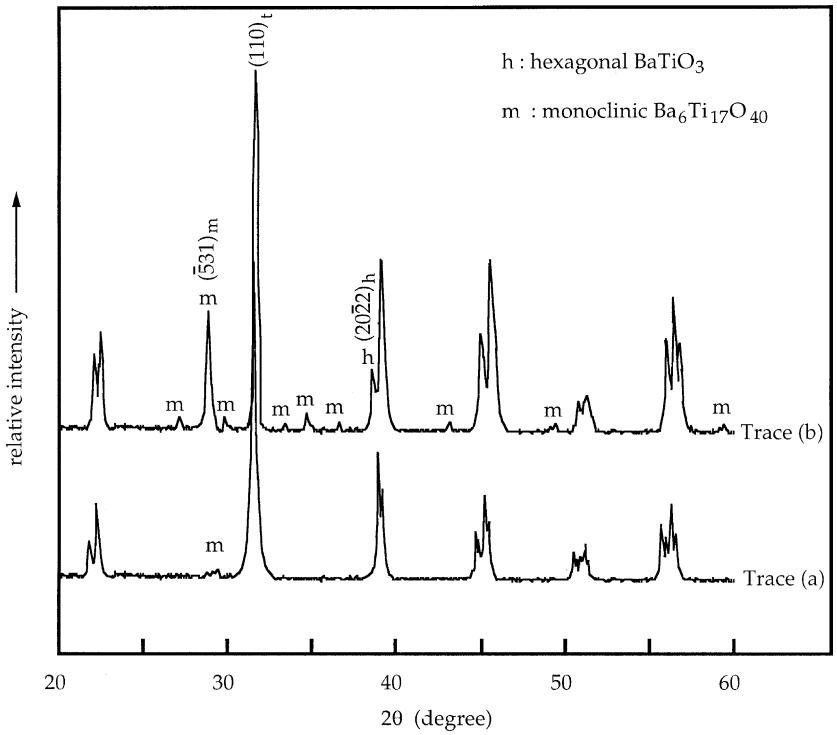

Fig. 2. XRD traces of (a) undoped and (b) SrO-doped $BaTiO_3$ samples sintered at 1400 °C.

(m-)$Ba_6Ti_{17}O_{40}$ (B_6T_{17}) second phase crystallised from the eutectic liquid formed at above 1332 °C [14]. This is shown in trace (a) of Fig. 2. The presence of B_6T_{17} is manifested in $(\bar{5}31)_m$, since the strongest $(\bar{1}33)_m$ reflection has overlapped with $(1\,1\,0)_t$ of $BaTiO_3$. Its existence is clearly detected from the Sr-doped samples (trace (b)). The metastable retention of hexagonal (h-)$BaTiO_3$ [15] has also occurred in the Sr-doped samples (as revealed by trace (b)). It can be unambiguously discerned from the hexagonal $(2\,0\,\bar{2}\,2)_h$ reflection. This peak has probably included $(0\,0\,0\,6)_h$ appearing in its proximity. Other reflections from the hexagonal phase, although of higher intensities, have merged with those of the tetragonal phase and become indistinguishable from the XRD trace. Doping with $SrTiO_3$

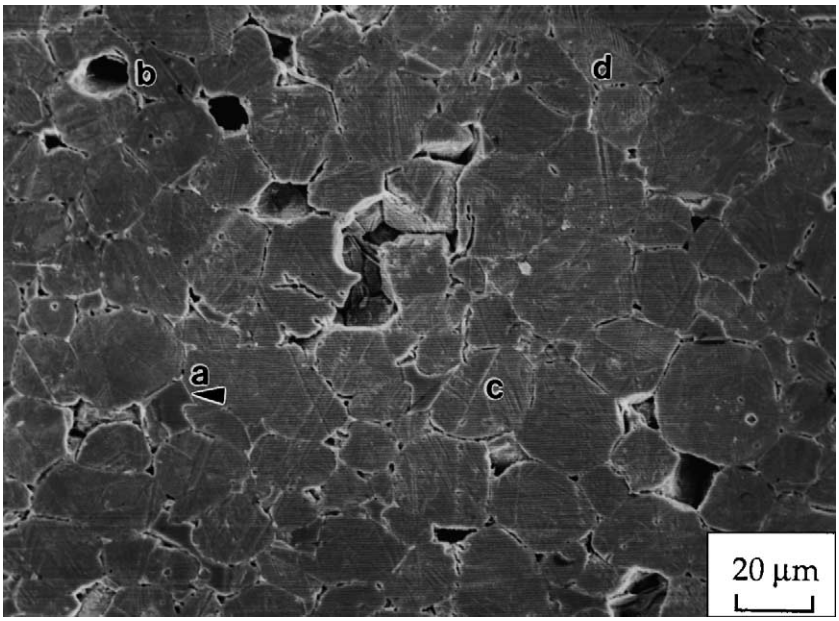

Fig. 3. Polished section of the Sr-doped $BaTiO_3$ ceramics showing the microstructural features of (a) second phase, (b) residual pores, (c) twinning and (d) ferroelectric domains (SEM-SEI).

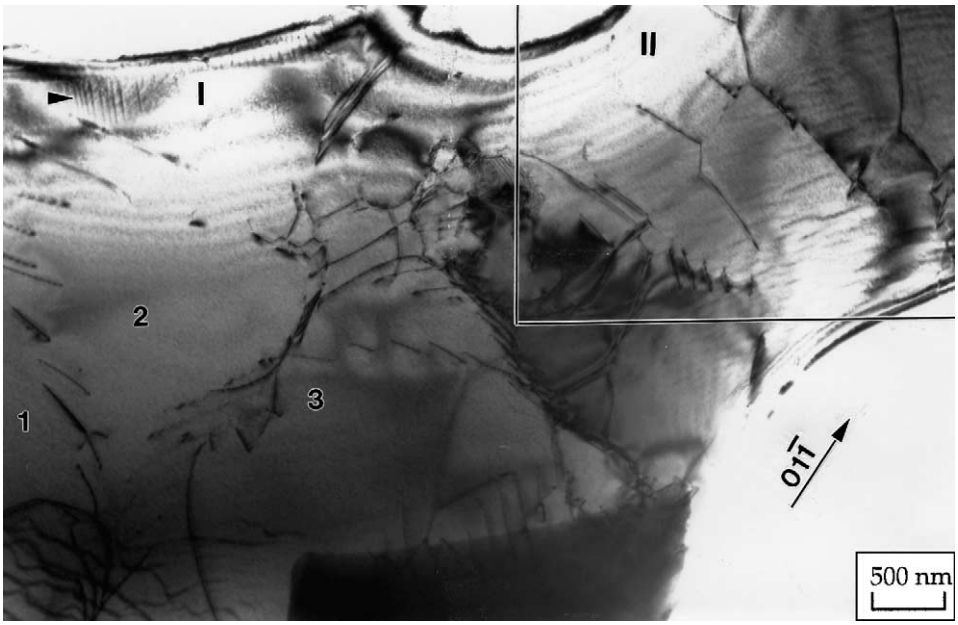

Fig. 4. A representative microstructure of the Sr-doped $BaTiO_3$ ceramics containing dislocations forming nodes, networks, tangles and low-angle grain boundaries (TEM-BF image).

has resulted in a systematic peak shift towards higher 2θ angle, e.g. $(1\,1\,0)_t$ indicating a contracted unit cell.

Second phases at the triple-grain junctions containing B_6T_{17}, suggested by the XRD trace (b) in Fig. 2, were also confirmed by the energy-dispersive spectroscopy (EDS) of X-ray equipped with SEM. The representative microstructure features in sintered samples are (a) second phase (of B_6T_{17}), (b) residual pores, (c) $\{1\,1\,1\}$ twins and (d) ferroelectric domains as indicated in Fig. 3.

3.2. Dislocations

Most of the dislocations found in sintered $BaTiO_3$, undoped as well as Sr-doped formed nodes, networks, tangles and low-angle grain boundaries (LAGBs). An example of $(Ba_{0.9}Sr_{0.1})TiO_3$, sintered at 1400 °C for 100 h, is shown in Fig. 4 where dislocations of the framed regions I and II have been further analysed for their Burgers vectors ($\boldsymbol{b}$) and line directions ($\boldsymbol{u}$).

Polygonisation has occurred as evidenced by the formation of sub-grains, notably of region I in Fig. 4. It is shown at a higher magnification in Fig. 5a where sub-grains of 1, 2 and 3, associated with dislocation arrays A, B, C and D, were in slightly different Bragg diffraction conditions. The LAGBs of sub-grains 1–2 and sub-grains 2–3 are ∼0.05° and ∼0.42°, respectively. The misorientation was estimated by measuring the amount of shift (Δ) off the exact Bragg diffraction condition of $Z = [1\,1\,1]$ for the individual sub-grains. The zone centre has moved along $[\bar{1}\,0\,1]$ by $\Delta \approx 8$ mm, as indicated in Fig. 5b, when shifting from sub-grains 2–3. The misorientation (θ) caused by dislocation arrays A and B can be calculated by adopting: $\Delta \approx L\theta$, where L is the camera length. The formation of LAGBs requires [16] both climb and glide of edge dislocations during dynamic recovery.

The dislocations in arrays A, B and C (as indicated in Fig 5a), were determined for the line directions ($\boldsymbol{u}$) and Burgers vectors ($\boldsymbol{b}$) by the invisibility criterion of $\boldsymbol{g} \cdot \boldsymbol{b} = 0$ and trace analysis. However, dislocation D was not determined for $\boldsymbol{u}$ and $\boldsymbol{b}$. Results are listed in Table 1. Dislocations marked with A and B are the pure edge type, where $\boldsymbol{u} \perp \boldsymbol{b}$ but they lie on different planes of $(0\,1\,1)$ and $(0\,1\,0)$, which are then the respective glide plane for dislocations in arrays A and B. Dislocation C is of a mixed character with the angle α of $\boldsymbol{u} \angle \boldsymbol{b} = 45°$ between dislocation line and Burgers vector. Further, its glide plane containing both $\boldsymbol{b}$ and $\boldsymbol{u}$ is likely to be $(1\,0\,0)$. The suggestion is that not only the $\langle 1\,0\,0\rangle\{0\,0\,1\}$ slip systems [4–12] have been activated by pressureless-sintering at 1400 °C, but also $\langle 1\,0\,0\rangle\{1\,1\,0\}$. Further, the deformation of $BaTiO_3$ at high temperatures has been contributed by gliding of edge dislocations along $\langle 1\,0\,0\rangle$ on $\{1\,1\,0\}$ as well as $\{0\,0\,1\}$. The present observation is consistent with those reported by both Doukhan and Doukhan [7] and Poirier et al. [4] for glide occurs similarly on the $\{1\,0\,0\}$ and $\{1\,1\,0\}$ planes [7], and dislocations

Table 1
Analysis of the dislocation line vectors and Burgers vectors associated with sub-grains

Dislocation	A	B	C
$\boldsymbol{b}$	$[1\,0\,0]$	$[0\,0\,1]$	$[0\,0\,1]$
$\boldsymbol{u}$	$[0\,1\,\bar{1}]$	$[1\,0\,0]$	$[0\,1\,1]$
Glide plane character	$[0\,1\,1]$	$[1\,0\,0]$	$[0\,1\,1]$
	Pure edge	Pure edge	45° mixed

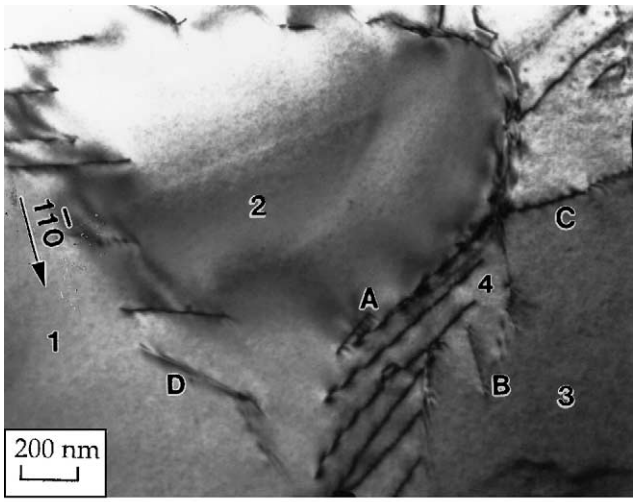

(a)

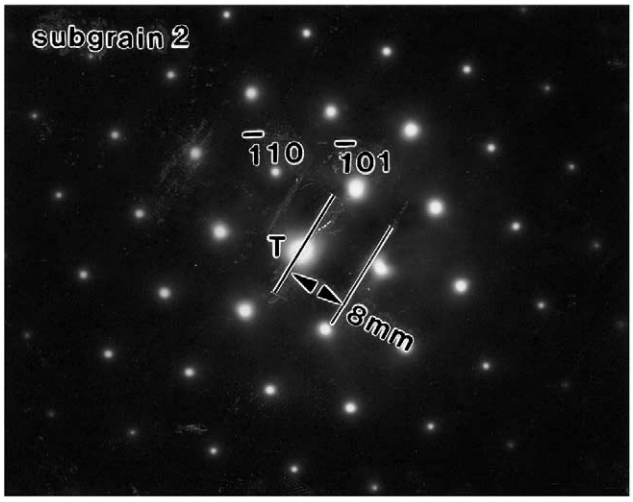

(b)

Fig. 5. (a) Two-beam BF images of dislocation arrays A, B and C with (b) the corresponding SADPs (TEM).

with $\boldsymbol{b}$=⟨1 0 0⟩ predominated [4] at high temperatures (of 1400 °C).

3.3. Nodes and networks

Region II of Fig. 4 at a higher magnification is given in Fig. 6a. Dislocations have met at a point and formed nodes whose Burgers vectors have been determined. In comparison, dislocation lines between the nodes of the dislocation network located in lower left corner (indicated with blank arrow in Fig. 6) have contracted [17] in much shorter lengths. The dislocations involved in forming the network of region II are those with the Burgers vectors of $\boldsymbol{b}$=⟨1 $\bar{1}$ 0⟩ as well as ⟨1 0 0⟩. It is illustrated schematically in Fig. 6b, where the dislocations lying in the same plane have reacted to form nodes and networks during sintering. The Burgers vectors of $\boldsymbol{b}_1 = [\bar{1}\,1\,0]$, $\boldsymbol{b}_2 = [\bar{1}\,1\,0]$ and $\boldsymbol{b}_3 = [0\,1\,0]$ are consistent with Frank's rule: $\boldsymbol{b}_1 = \boldsymbol{b}_2 + \boldsymbol{b}_3$.

3.4. Dissociated dislocations

Fig. 7 presents the $\boldsymbol{g}$-4$\boldsymbol{g}$ WBDF images of dislocations with $\boldsymbol{b} = \langle 0\,1\,0\rangle$ and $\langle 1\,1\,0\rangle$, respectively, in the Sr-doped samples sintered at 1400 °C for 100 h. No dislocation dissociations to collinear partials as those reported for $SrTiO_3$ [9] and $BaTiO_3$ [11] or the scallop-shaped half-partials as those also reported for $BaTiO_3$ [7,11,12] can be discerned in samples subjected to prolonged sintering at 1400 °C.

However, dislocations containing a series of small half-loop partials resembling scallops [7,11,12] have been observed in both undoped $BaTiO_3$ and Sr-doped $BaTiO_3$ sintered at 1400 °C for a shorter sintering of 10 h. The dissociated dislocations are consisted of three segments with Burgers vectors following the reaction: $\boldsymbol{b}_1 = \boldsymbol{b}_2 + \boldsymbol{b}_3$, where $\boldsymbol{b}_2$ and $\boldsymbol{b}_3$ are the partial dislocations dissociated from the perfect dislocation $\boldsymbol{b}_1$. The black dots, likely to be dislocation loops, and seen ubiquitously in samples sintered at >1400 °C [18] as indicated by empty arrows in Fig. 8b, have been analysed and reported in another manuscript.

The dissociation reaction [7] for dislocation 1, as labelled in Fig. 8a, may be described by

$$[0\,0\,1] \rightarrow \tfrac{1}{2}[1\,0\,1] + \tfrac{1}{2}[\bar{1}\,0\,1] \quad (6)$$

where $\boldsymbol{b}_1$ = [0 0 1] (the original dislocation), $\boldsymbol{b}_2$ = 1/2[1 0 1] and $\boldsymbol{b}_3$ = 1/2[$\bar{1}$ 0 1] (the scallop-shaped half-partials).

Dissociation by pure glide may have occurred in (0 1 0), and by pure climb in (1 0 0) or (0 0 1) [4,8].

The dissociated segment, $\boldsymbol{b}_1'$, of dislocation 2 (as labelled in Fig. 8a and referred to Fig. 8c) exhibits only residual contrast (as indicated by arrows). It also reveals that $\boldsymbol{b}_2$ of dislocation 1 (as indicated by arrows) containing a series of half-loops [7,11,12] is effectively invisible. Similarly, the segment of perfect dislocation $\boldsymbol{b}_1$ in dislocation 1 appears invisible as indicated by arrows in Fig. 8b. So does the $\boldsymbol{b}_2'$ segment of dislocation 2 in Fig. 8b. The seemingly dissociated $\boldsymbol{b}_1$ is a double image (as indicated by arrows) due to the two-beam condition was not strictly adhered, as is also evidenced by the whole dislocation line (Fig. 8b).

Dissociation reactions derived from the Burgers vectors determined for the two scallop-shaped half-partials labelled 1 and 2 in Fig. 8a and b have other possibilities. One for dislocation 1 as described earlier (Eq. (6)) and the other [7,9] for dislocation 2 is then

$$[1\,0\,1] \rightarrow [0\,0\,1] + [1\,0\,0] \quad (7)$$

where $\boldsymbol{b}_1' = [1\,0\,1]$, $\boldsymbol{b}_2' = [0\,0\,1]$ and $\boldsymbol{b}_3' = [1\,0\,0]$.

Dissociation by pure glide may also take place on (0 1 0) in which the Burgers vector $\boldsymbol{b}_1' = [1\,0\,1]$ of the perfect dislocation and the two dissociated ones, $\boldsymbol{b}_2'$ and $\boldsymbol{b}_3'$, lie. That is to say, dissociation of $\boldsymbol{b}_1'$ may have occurred in plane (0 1 0) containing the Burgers vectors of the three dislocations in

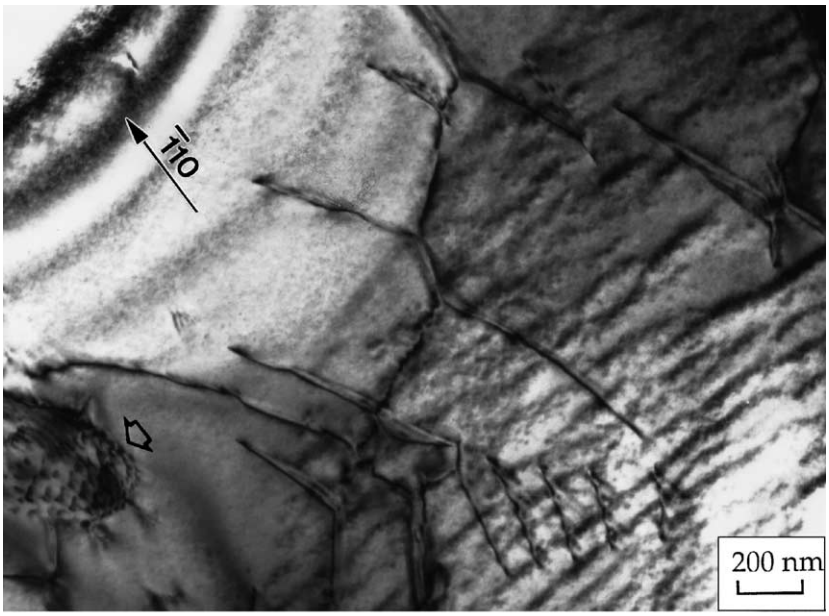

(a)

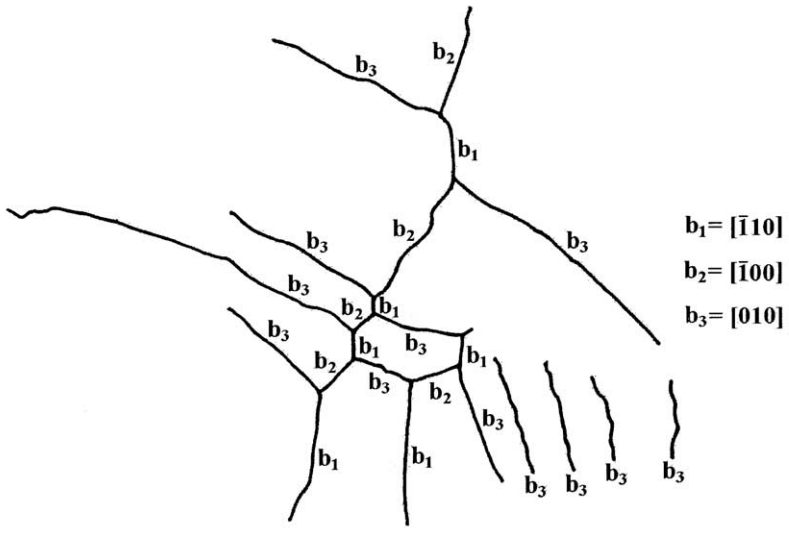

(b)

Fig. 6. Dislocations forming nodes and networks in (a) two-beam BF image (TEM) and (b) the schematic illustration correspondingly.

Eq. (7). Pure climb dissociation may take place in a plane whose normal is perpendicular to [0 1 0], i.e. in the (1 0 0) or (0 0 1) plane. It has been suggested [4] that dissociation occurs in the perovskites [7,9] in planes other than the slip planes when dislocations move in a non-conservative fashion.

The scallop-shaped segments from the dissociated dislocations, shown in Fig. 8a and b, have two distinctive Burgers vectors of $\boldsymbol{b}_3 = 1/2[\bar{1}\,0\,1]$, similar to previously reported [7,12], and $\boldsymbol{b}'_3 = [1\,0\,0]$.

The dissociated dislocations 1 and 2 with the respective Burgers vectors are illustrated schematically in Fig. 8c.

4. Discussion

4.1. Dislocation dissociations

Plastic deformation by glide along $\langle 1\,1\,0\rangle$ and $\langle 0\,0\,1\rangle$ in $\{1\,1\,0\}$ and $\langle 0\,0\,1\rangle$ in $\{1\,0\,0\}$, as reported before for single-crystal [4,7] as well as polycrystalline $BaTiO_3$ [12], and other perovskites [6], have also occurred in samples pressureless-sintered at 1400 °C for 10 h.

The dissociation of dislocation 1 in Fig. 8a and b by Eq. (6) is identical to that reported by Doukhan and Doukhan [7]. Similarly, the suggestion is also that the half-loop partial of $\boldsymbol{b}_3 = 1/2[\bar{1}\,0\,1]$ has escaped from (0 0 1) with the other

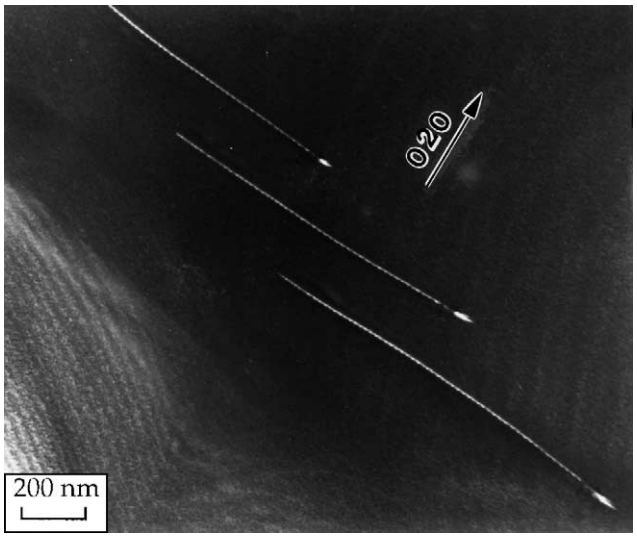

Fig. 7. Dislocations in Sr-doped $BaTiO_3$ samples sintered at 1400 °C for 100 h revealed no dissociations, $\boldsymbol{b} = \langle 1\,1\,0 \rangle$ ($\boldsymbol{g}$-4$\boldsymbol{g}$ WBDF images, TEM).

partial of $\boldsymbol{b}_2 = 1/2[1\,0\,1]$ still lying on it (as illustrated in Fig. 1).

Dissociation starting from cusps, which exhibited strong contrast under TEM, along the dislocation lines of $\boldsymbol{b}_1' = [\bar{1}\,0\,1]$ was proposed [7], but without convincing experimental evidence. The "cusps", if existed, further dissociated into similar scallop-shaped half-partials are unambiguously demonstrated by dislocation 2 in Fig. 8a and b. Dislocation 2 has followed the dissociation reaction as suggested [7] for dislocations with $\boldsymbol{b} = \langle 1\,\bar{1}\,0 \rangle$ which contained cusps in deformed $BaTiO_3$ single crystals. The dissociation of $\boldsymbol{b}_1'$ into scallop-shaped half-partials occurred in the cusps of dislocations with $\boldsymbol{b}_3' = [1\,0\,0]$ escaping [7] from the (1 0 0) or (0 0 1) plane. The dissociation reaction is described by Eq. (7). The dissociation plane of (1 0 0) or (0 0 1) may have been similar to those of dislocation 1 as was also reported by Doukhan et al. The dissociation (of Eq. (7)), however, would not lead to any significant reduction in the energy per unit length of dislocations.

Because the line directions for all dislocations in Fig. 8a and b were not determined, whether their dissociation had taken place by climb [7,9], glide [9] or a mixed mechanism [11,12] cannot be confirmed at the present time.

4.2. Recovered microstructure

The microstructure shown in Fig. 4 consisting of dislocation nodes, networks (region II) and sub-grains (region I) represents that the grains deformed by pressureless-sintering were undergoing dynamic recovery. Dislocation climb from the slip planes results in the formation of LAGBs, as shown in Fig. 5a, whereby the total strain energy is reduced. The long-range strain becomes localised in the proximity of dislocations. Sufficient local and long-range lattice diffusion via vacancies leading to dislocation climb has facilitated

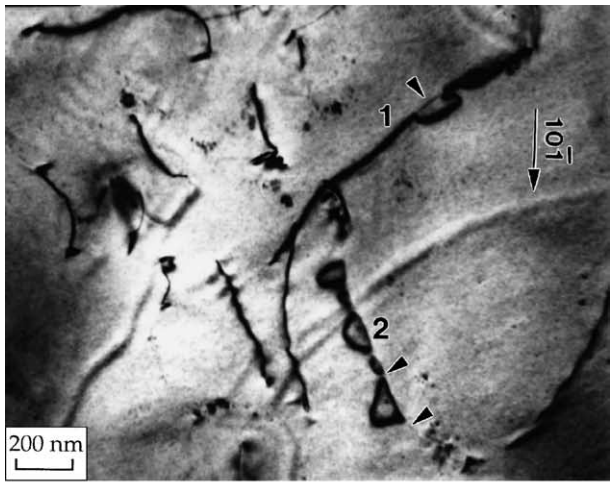

(a)

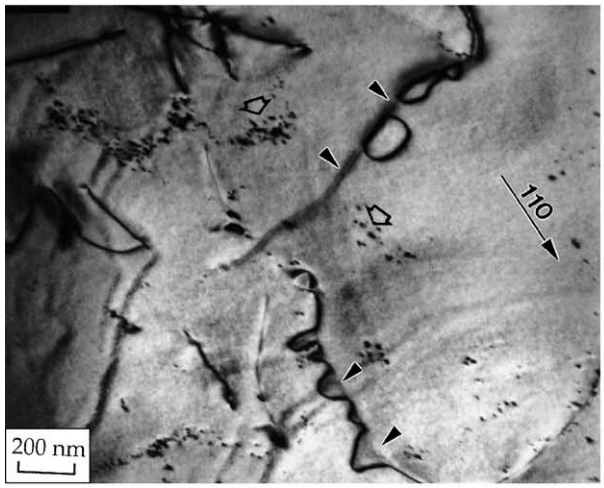

(b)

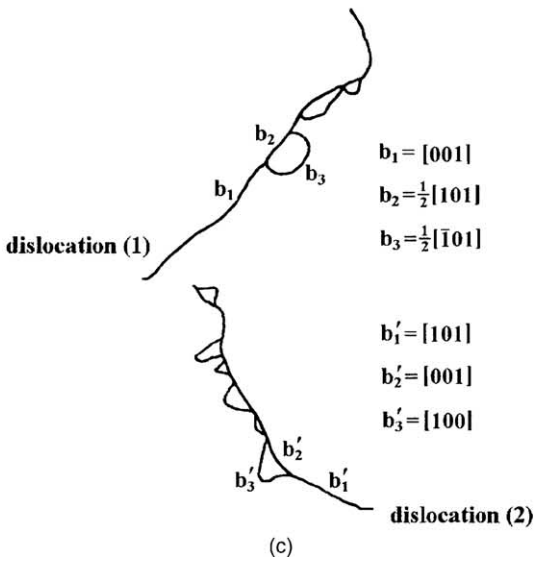

(c)

Fig. 8. Dislocations contain a series of small scallop-shaped half-loop partials from two-beam BF images of (a) $\boldsymbol{g} = 10$, (b) $\boldsymbol{g} = 110$ (TEM) and (c) the schematic illustration for the dissociation reaction in dislocations 1 and 2.

the dynamic recovery at 1400 °C. Polygonisation forming sub-grains started upon the local rearrangement of dislocations, which have been generated by the intrinsic sintering stress (Σ). The plastic deformation took place particularly in the initial stage of sintering [1] (as will be addressed below).

A sub-grain cell 4, apart from 1, 2 and 3, may also exist between the arrays of dislocations A and B as shown in Fig. 5a. The tilt boundary of $\theta \approx 0.42^{\circ}$ determined for Fig. 5a and b has considered the dislocation arrays of A and B as a whole. Since $\boldsymbol{b}_A = [1\,0\,0]$ and $\boldsymbol{b}_B = [0\,0\,1]$ are both of the pure edge type (cf. Table 1), sub-grain boundaries separating 2–4 and 4–3 by dislocation arrays A and B, consisting of pure edge dislocation arrays, are the systematical tilt boundaries [18].

Both glide and climb must have occurred to facilitate sub-grain formation at 1400 °C [16,17]. Atom diffusion via lattice defects generated thermally in $BaTiO_3$ are likely to be the intrinsic Schottky type consisting of cation and anion vacancies, V''_{Ba}, V''''_{Ti} and $V_O^{\bullet\bullet}$ [19]. The fact that extensive dislocation climb has facilitated sub-grain formation during polygonisation (Figs. 4 and 5) supports the existence of a high concentration of thermal vacancies when $BaTiO_3$ was sintered at 1400 °C.

4.3. Implications to densification mechanisms

Plastic flow was thought by Ogbuji et al. [1] to have contributed to densification in ceramic sintering, although others [20,21] concluded that its contribution was insignificant comparing to those by diffusion processes in pressureless-sintering. The sintering of ceramics may be conceived as high-temperature deformation driven by the thermodynamic driving force of $\Delta p = \gamma_{sv}/\rho$, where γ_{sv} is the surface-to-vapour surface energy and ρ is the neck curvature, which is originated from the net neck curvature ($\sim 1/\rho$) [22]. Sintering can be differentiated from high-temperature creep since the effective stress (sometimes called the sintering stress (Σ)) translated from the chemical potential gradient ($\Delta\mu$) into the form of a pressure difference (Δp, the thermodynamic driving force) is not a constant but strongly depends upon the sintered density (or, equivalently, residual porosity) [23,24]. The thermodynamic driving force is being consumed, and so reduced, continuously upon the sintering of the ceramic, densification as well as coarsening.

The slip systems of $\langle 1\bar{1}0\rangle\{1\,1\,0\}$, $\langle 1\,0\,0\rangle\{1\,1\,0\}$ and $\langle 1\,0\,0\rangle\{0\,0\,1\}$ in $BaTiO_3$ have been activated by the action of Δp, as evidenced from the microstructure observed. They are formed particularly in the initial stage when neck curvature is at its smallest. Dislocations are generated when Δp is at its largest, and distributed randomly on the slip planes of both $\{0\,0\,1\}$ and $\{1\,1\,0\}$. Acting on the grain-boundary plane to push two grains closer together, the driving force then brings about overall system shrinkage via plastic deformation at high temperatures. The resultant effective stress intensified by neck curvature [1] must therefore exceed the critical resolved shear stress (CRSS) to have activated the relevant slip systems in $BaTiO_3$, as evidenced by the observations, but the exact values of CRSS not available in the literature will have to be determined by deforming single crystals as in sapphire [25].

Plastic deformation is important in the sintering of ceramics for it has contributed to the overall densification by activating the slip systems in $BaTiO_3$. Nevertheless, even when densification, particularly in the initial stage, has occurred and been contributed by dislocation mechanisms, the overall sintering rate could still be determined by lattice diffusion in climb-controlled dislocation glide [26]. Indeed, pressureless-sintering kinetics of $BaTiO_3$ suggested [19] that the rate-determining mechanism for sintering is the lattice diffusion of Ba^{2+} via vacancies.

5. Conclusions

Pressureless-sintering at 1400 °C has activated the slip systems of $\langle 1\,\bar{1}\,0\rangle\{1\,1\,0\}$, $\langle 1\,0\,0\rangle\{1\,1\,0\}$ and $\langle 1\,0\,0\rangle\{0\,0\,1\}$ in $BaTiO_3$. The stresses resulting in the plastic deformation of $BaTiO_3$ are attributed to the thermodynamic driving force (Δp) intensified by the neck curvature amongst powder particles, particularly in the initial stage of sintering when Δp is relatively large. Dislocations are dissociated by a climb mechanism into the scallop-shaped half-loop partials by either of the two reactions of: $[1\,0\,1] \rightarrow [0\,0\,1] + [1\,0\,0]$ and $[0\,0\,1] \rightarrow 1/2[1\,0\,1] + 1/2[\bar{1}\,0\,1]$. Dynamic recovery takes place when polygonisation has begun at 1400 °C.

Acknowledgements

Funding by the National Science Council of Taiwan through Contract Numbers NSC 89-2216-E-110-009, 89-2216-E-110-037 and 90-2216-E-110-018 is acknowledged.

References

[1] L. Ogbuji, T.E. Mitchell, A.H. Heuer, Plastic deformation during the intermediate stage of sintering, in: G.C. Kuczynski (Ed.), Materials Science Research, vol. 13, Plenum Press, New York, 1980, pp. 135–140.
[2] D.L. Anderson, The Earth as a planet: paradigms and paradoxes, Science 223 (1984) 335–347.
[3] L.G. Liu, Phase transformations and the construction of the deep mantle, in: M.W. Elhinny (Ed.), The Earth, its Origin, Structure and Evolution, Academic Press, New York, 1979, pp. 117–202.
[4] J.P. Poirier, S. Beauchesne, F. Guyot, Deformation mechanisms of crystals with perovskite structure, in: A. Navrotsky, D.J. Weidner (Eds.), Perovskite: A Structure of Great Interest to Geophysics and Materials Science, American Geophysical Union, Washington, DC, 1989, pp. 119–23.
[5] Y. Wang, F. Guyot, A. Yeganeh-Haeri, R.C. Liebermann, Twinning in $MgSiO_3$ perovskite, Science 248 (1990) 468–471.
[6] J.P. Poirier, J. Peyronneau, J.Y. Gesland, G. Brebec, Viscosity and conductivity of the lower mantle; an experimental study on a $MgSiO_3$

perovskite analogue, $KZnF_3$, Phys. Earth Planet. Interiors 32 (3/4) (1983) 273–287.
[7] N. Doukhan, J.C. Doukhan, Dislocations in perovskite $BaTiO_3$ and $CaTiO_3$, Phys. Chem. Miner. 13 (1986) 403–410.
[8] J. Nishigaki, K. Kuroda, H. Saka, Electron microscopy of dislocation structures in $SrTiO_3$ deformed at high temperatures, Phys. Status Solidi (A) 128 (1991) 319–336.
[9] Z. Mao, K.M. Knowles, Dissociation of lattice dislocations in $SrTiO_3$, Philos. Mag. A 73 (3) (1996) 699–708.
[10] Y. Wang, J.-P. Poirier, R.C. Liebermann, Dislocation dissociation in $CaGeO_3$ perovskite, Phys. Chem. Miner. 16 (1989) 630–633.
[11] M.H. Lin, H.Y. Lu, Collinear partial dislocations in barium titanate perovskite, Mater. Sci. Eng. A333 (1/2) (2002) 41–44.
[12] M.H. Lin, H.Y. Lu, Dislocation substructures in CO_2-laser-sintered barium titanate, Phys. Status Solidi (A) 191 (1) (2002) 58–66.
[13] M.H. Lin, H.Y. Lu, Densification retardation in the sintering of La_2O_3-doped barium titanate ceramic, Mater. Sci. Eng. A323 (1/2) (2002) 167–176.
[14] K.W. Kirby, B.A. Wechsler, Phase relations in the barium–titanium oxide system, J. Am. Ceram. Soc. 74 (8) (1991) 1841–1847.
[15] M.H. Lin, H.Y. Lu, Hexagonal-phase retention in pressureless-sintered $BaTiO_3$, Philos. Mag. A 81 (1) (2001) 181–196.
[16] D. Hull, D.J. Bacon, Introduction to Dislocations, 3rd ed., Pergamon Press, Oxford, 1984, pp. 175–209.
[17] D. Callaird, J.L. Martin, Microstructure of aluminium during creep at intermediate temperature. I. Dislocation network after creep, Acta Metall. 30 (3) (1982) 437–445.
[18] C.Y. Chen, H.Y. Lu, Dislocation loops in pressureless-sintered undoped $BaTiO_3$ ceramics, unpublished results.
[19] M.H. Lin, Y.F. Chou, H.Y. Lu, The rate-determining mechanism in the sintering of undoped nonstoichiometric $BaTiO_3$, J. Eur. Ceram. Soc. 20 (4) (2000) 516–527.
[20] M.F. Ashby, A first report on deformation mechanism maps, Acta Metall. 20 (1972) 887–897.
[21] R.L. Coble, R.M. Cannon, Recent paradigms in powder processing, in: H. Palmour III, R.F. Davies, T.M. Hare (Eds.), Materials Science Research, vol. 11, Plenum, New York, 1978, pp. 151–170.
[22] Y.M. Chiang, D. Bernie III, W.D. Kingery, Physical Ceramics: Principles for Ceramic Science and Engineering, Wiley, New York, 1997, pp. 392–428.
[23] R.L. Coble, Diffusion models for hot-pressing with surface energy and pressure effects as driving force, J. Appl. Phys. 41 (12) (1970) 4787–4807.
[24] A.S. Helle, K.E. Easterling, M.F. Ashby, Hot-isostatic pressing diagrams: new developments, Acta Metall. 33 (12) (1985) 2163–2174.
[25] K.P.D. Lagerlof, A.H. Heuer, J. Castaing, J.P. Riviere, T.E. Mitchell, Slip and twinning in sapphire, J. Am. Ceram. Soc. 77 (2) (1994) 385–397.
[26] J.P. Poirier, Creep of Crystals, Cambridge University Press, Cambridge, 1985, pp. 94–144.